Low-frequency picotesla field detection with planar Hall effect bridge sensors

A. Persson[1], R. Bejhed[2], K Gunnarsson[2], H. Nguyen[1], B. T. Dalslet[3], F. W. Østerberg[3], M. F. Hansen[3], and P. Svedlindh[2]
[1]Ångström Space Technology Centre, Uppsala University, Ångström Laboratory Box 534 SE-75121, Uppsala, Sweden
[2]Division of Solid State Physics, Dept. of Engineering Science, Uppsala University , Ångström Laboratory Box 534 SE-75121, Uppsala, Sweden
[3]Dept. of Micro- and Nanotechnology, Technical University of Denmark, DTU Nanotech, Building 345 East, DK-2800 Kongens Lyngby, Denmark

Abstract

The applicability of miniaturized magnetic field sensors are being explored in several fields of magnetic field detection, due to their integratability, low mass, and potentially low cost. In this respect, different thin-film technologies, especially those employing magnetoresistance, show great potential, being compatible with micro- and nanotechnology batch processing. For low-frequency magnetic field detection, sensors based on the planar Hall effect, especially planar Hall effect bridge (PHEB) sensors, show promising performance given their inherent low-field linearity, limited hysteresis and moderate noise figure. In this work, the applicability of such PHEB sensors to different areas is investigated. An analytical model was constructed, to estimate the performance of an arbitrary PHEB in terms of e.g. sensitivity and detectivity. The model incorporates a number of approximations and, to validate the results, modelled data is compared to measurements on actual PHEBs. It is concluded that the model slightly underestimated the detectivity, especially at low frequencies and when demagnetizing effects becomes apparent. The model is also sensitive to fabrication process induced variations of the material parameters of the sensors. Nevertheless, accounting for these discrepancies, the modelled data is typically within 10% from the experimental data and the model can be used to estimate the performance of a particular PHEB design. The model is also used to establish a design process for optimizing a PHEB to a particular set of requirements on the bandwidth, detectivity, compliance voltage and amplified signal-to-noise ratio. By applying this design process, the size, sensitivity, resistance, bias current and power consumption of the PHEB can be calculated. The model shows that

PHEBs are applicable to several different science areas including archaeological surveying, satellite attitude determination, scientific space missions, and magnetic bead detection in lab-on-a-chip applications.

Introduction

Ever since the invention of the compass in 11th century China [1], magnetic field sensors have come to be essential in an increasing number of areas. Nowadays, magnetic sensor systems, or magnetometers, are employed in e.g., electronic compasses [2, 3], archaeological surveys [4, 5], different space applications [6-8], and as bio-sensors [9, 10]. Two key features in a magnetic sensor are the field range and the detectivity, i.e., the maximum and minimum field strength the sensor can accurately detect. The linear field range and detectivity of some commercial magnetic sensors are presented in figure 1, along with their applications.

In most of the applications requiring detectivities of less than 100 pTHz$^{-0.5}$ at 1 Hz bulky instruments, such as fluxgates and different kinds of optically pumped magnetometers, have been the only viable option [4-7]. However, in recent years miniaturized versions of these instruments have emerged, with a total system mass of around 0.1 kg [11, 12]. Nevertheless, reducing the mass further has proven difficult, and an the interest for different thin-film magnetic field sensors, such as magnetoresistance, has therefore increased, since these allow for extreme miniaturization due to their inherent compatibility with micro- and nano-structuring techniques [13].

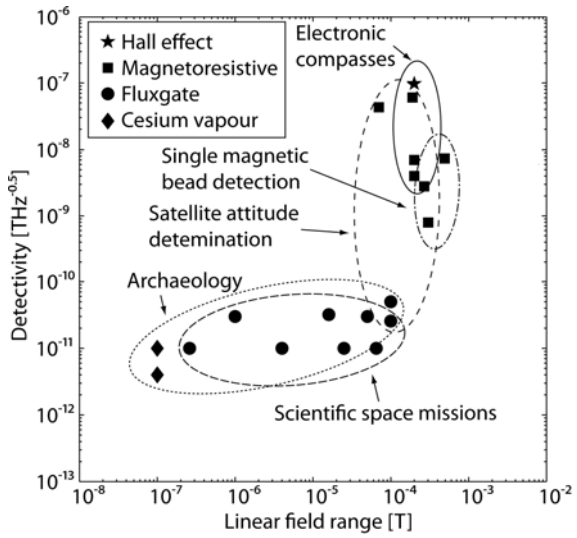

Figure 1. Linear field range and detectivity of some magnetometers and magnetic field sensors, along with their applications.

In space applications, magnetoresistive sensors based on anisotropic magnetoresistance (AMR) [14], giant magnetoresistance (GMR) [15], and tunnelling magnetoresistance (TMR) [16] have been proposed. However, their inherent low-frequency noise has this far limited them to less sensitive attitude determination systems [17], and in radiation tolerant memory circuits [18]. Other disadvantages with magnetoresistive sensors are their relatively poor linearity and pronounced hysteresis, requiring the sensors to be biased with an external magnetic field. However, a magnetoresistive sensor with sufficient detectivity would, potentially, reduce the system mass with more than two orders of magnitudes, as compared to miniaturized fluxgates, given its simple function not requiring any complicated supporting electronics. Such a magnetometer would not only allow for small satellites to be equipped with highly sensitive magnetometers, but also for completely new types of missions such as high-resolution mapping of small-scale magnetic features, e.g., Alfvénic turbulence, by one or many satellites equipped with hundreds of distributed magnetometers [19].

In the field of medicine there is a constant search for more sensitive and reliable diagnostic methods [20, 21]. In some cases only infinitesimal amounts of a certain substance separate a positive from a negative sample. The presence of this substance needs to be translated into something that can be measured. One way to approach this is to use magnetic biodetection utilizing magnetic nanoparticles. The particles become magnetized when exposed to an external magnetic field and their surface can be functionalized so that it reacts specifically with the substance in question [22]. If the sample is positive the reaction takes place and the hydrodynamic volume and thus the Brownian rotation frequency of the particle will be affected to a degree that could be picked up by a small magnetic field sensor [23, 24]. These kinds of measurements typically take place at frequencies ranging from 1Hz to 100kHz, which requires a sensor with low noise within this frequency interval. In order to get a meaningful read-out, ten thousand to hundred thousand particles are measured upon simultaneously, covering a surface of approximately 100 μm × 100μm [25, 26]. For a monodisperse nanoparticle ensemble with $N_p = 10^5$ particles and a particle diameter of 100 nm, applying an AC magnetic field with amplitude 1 mT, the magnetic field due to the ensemble of particles after sedimentation is typically about 0.51 μT (calculation summarizing the dipole field contributions from all particles). The position of a particle with respect to the sensor area is an important error factor. The effect of this is mitigated by using a large enough ensemble of particles and a sensor covering the same area as the particle ensemble in combination with a shallow microfluidic channel in which the sensor is placed. In such a case, with the particles statistically distributed over the sensor area, one may expect that the error in the measured magnetic field should scale as $N_p^{-1/2}$.

Among the magnetoresistive sensor techniques, sensors based on the planar Hall effect (PHE) have started to generate much interest. These employ

the off-diagonal terms of the magnetic field-dependent resistivity tensor of an AMR sensor [27, 28]. PHE sensors have an intrinsically linear low-field response with little hysteresis, combined with a relatively moderate low-frequency noise as compared to, e.g., GMR and TMR sensors [29, 30]. Moreover, if structured in a Wheatstone bridge configuration, it has been shown that the sensor output can be enhanced by more than a factor of 100, as compared to the traditional cross-shaped designs [31]. Here, the applicability of such PHE bridge (PHEB) sensors to low-frequency magnetic field measurements is investigated by constructing an analytical model for the detectivity of an arbitrary PHEB sensor design. The model is also implemented to find the optimum design of a PHEB, given certain requirements on detectivity, bandwidth, etc. The modelled data was also compared with results obtained from measurements on PHEB sensors to evaluate the validity of the model.

Theory

The PHE voltage, V_y, of a single-domain, cross-shaped PHE sensor, magnetized in-plane along the unit vector $\hat{\mathbf{m}} = (\cos\theta, \sin\theta)$, where θ is the angle between the magnetization vector and the anisotropy axis, is given by:

$$V_y^{\text{cross}} = I\Delta\rho\sin(2\theta)(2t_{\text{FM}})^{-1}, \tag{1}$$

where I is the uniform current though the sensor with thickness, t_{FM}, $\Delta\rho = \rho_{\parallel} - \rho_{\perp}$ is the difference in resistivity with the magnetization parallel and perpendicular to I [29].

The PHE voltage can be increased by structuring the sensor in a Wheatstone bridge configuration, having branches at $\alpha = \pm 45$ where α is the angle between the branch current vector and the anisotropy axis [31]. The PHE voltage of a single segment PHEB is given by:

$$V_{\text{y}}^{\text{PHEB}} = (lI\Delta\rho\sin(2\theta))(2wt_{\text{FM}})^{-1}, \tag{2}$$

where l is the length and w is the width of each branch in the bridge [31].

To improve the signal-to-noise ratio of the bridge even further, each branch can be made up of a number of segments, N, all with length l and width w, connected in series or parallel. The PHE voltage of a PHEB with m segments connected in parallel and n such parallel constellations connected in series, i.e. $N=mn$, is given by:

$$V_{\mathrm{y}} = \left(nlI\Delta\rho\sin\left(2\theta\right)\right)\left(2mwt_{\mathrm{FM}}\right)^{-1}, \tag{3}$$

Assuming the PHEB to be exchange biased along the *x* axis, figure 2, the sensitivity, Σ, at small magnetic fields, H_{y}, is given by:

$$\Sigma\left[\mathrm{VT}^{-1}\right] = \mu_0^{-1}\left(\partial V_{\mathrm{y}}/\partial H_{\mathrm{y}}\right) = \left[nlI\ \Delta\rho\right]\cdot\left[mwt_{\mathrm{FM}}\left(H_{\mathrm{ex}} + H_{\mathrm{K}} + H_{\mathrm{d}}\right)\right]^{-1}, \tag{4}$$

where H_{ex}, H_{K} and H_{d} are the exchange-bias, anisotropy and demagnetizing fields, respectively [31, 32].

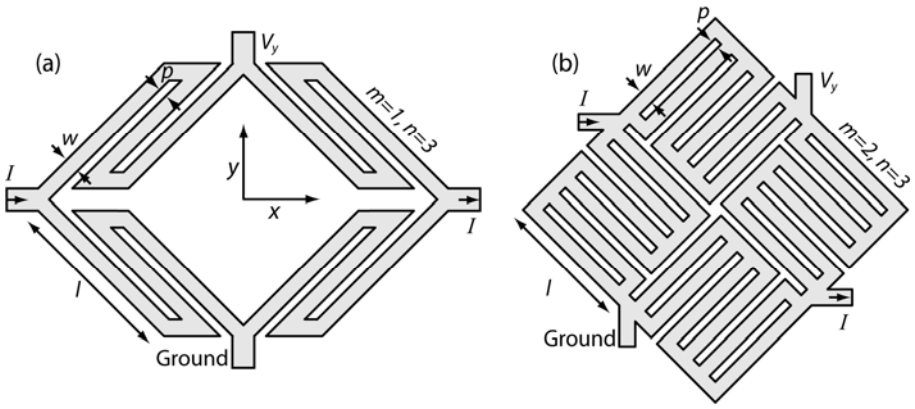

Figure 2. Two designs (a) and (b) of PHEBs with branches consisting of $N=mn$ segments of length l and width w, separated by a distance p. PHEBs A1-A7 and B1-B7 were of design (a).

The two most prominent noise sources inherent to a PHEB are thermal noise and $1/f$ noise. Here, the first dominates at high frequencies and the latter at low frequencies. The two noise domains are separated by the so called knee frequency, f_{k}. The power spectral density (PSD) of the thermal noise is given by the Johnson-Nyquist equation:

$$S_{\mathrm{T}}\left[\mathrm{V}^2\mathrm{Hz}^{-1}\right] = 4k_{\mathrm{B}}TR, \tag{5}$$

where k_{B} is Boltzmann's constant, T is the temperature, and $R=\rho nl(mwt_{\mathrm{FM}})^{-1}$, ρ being the resistivity of the PHEB branches [33]. The PSD of the $1/f$ noise is described by the phenomenological Hooge equation:

$$S_{1/f}\left[\mathrm{V^2Hz^{-1}}\right]=V^2\gamma_{\mathrm{H}}\left(N_{\mathrm{C}}f\right)^{-1}, \tag{6}$$

where $V=IR$, γ_{H} is the dimensionless Hooge parameter, $N_{\mathrm{C}}=n_{\mathrm{C}}mnlwt_{\mathrm{FM}}$ is the number of charge carriers, n_{C} is the charge-carrier density, and f is the frequency [34].

The detectivity of a PHEB sensor is given by the ratio between the voltage noise and the sensitivity and is given by:

$$D_{\mathrm{B}}\left[\mathrm{THz^{-1/2}}\right]=S_V^{1/2}\Sigma^{-1}=\left(S_{\mathrm{T}}+S_{1/f}\right)^{1/2}\Sigma^{-1}, \tag{7}$$

where S_{V} is the total inherent noise PSD of the PHEB [13].

Materials and methods

In this study, two sets of seven PHEB sensors each, labelled A and B, were examined. The sets differed with regard to the thickness of the current carrying, ferromagnetic NiFe layer, t_{FM}, which for set A was 30 nm and for set B was 45 nm thick. The design of the sets A and B can be seen in figure 2 (a).

The PHEBs were structured, using UV-lithography and lift-off, from a thin-film stack deposited by magnetron sputtering on a thermally oxidized Si wafer. The thin film stack had four layers, top down; Ta(5 nm) / $Ni_{80}Fe_{20}$ (30 nm or 45 nm) / $Mn_{76}Ir_{24}$ (20 nm) / Ta(5 nm), where subscripts denote the concentration in at. % and numbers in parentheses denote the film thickness. In order to define the direction of the easy axis of the NiFe layer, and the exchange coupling between the NiFe and MnIr layers, a magnetic field of 20 mT was applied along the x axis during sputtering (figure 2 (a)). Each PHEB consisted of N number of segments connected in series, i.e. $n=N$ and $m=1$, of length l and width w, making Nl the total length of a PHEB branch. The 14 PHEBs (7 + 7) from set A and B differed with regards to either t_{FM}, l or N according to table 1.

Before being characterized, the PHEBs were attached to a printed circuit board through wire bonding. The sensitivity of a PHEB sensor was calculated from the in-phase component of the PHE voltage while sweeping the magnetic field along the y axis between $\mu_0H_{\mathrm{y}}=\pm40$ mT along the y axis, figure 1 (a). The sensors were biased with an alternating current $I_{\mathrm{p\text{-}p}}\sin(2\pi ft)$ with $I_{\mathrm{p\text{-}p}}=1$ mA and $f=2.2$ kHz using a Keithley 6221 current source. The PHE voltage was amplified 40 dB by a Stanford Research Systems (SRS) SRS552 preamplifier and measured by an SRS SR830 lock-in amplifier.

Table 1. Thickness, length and number of segments, with n=N and m=1, of the PHEB of sets A and B.

PHEB	t_{FM} [nm]	l [μm]	N
A1	30	300	1
A2	30	450	1
A3	30	600	1
A4	30	750	1
A5	30	600	3
A6	30	600	5
A7	30	600	7
B1	45	300	1
B2	45	450	1
B3	45	600	1
B4	45	750	1
B5	45	600	3
B6	45	600	5
B7	45	600	7

For the noise measurements, a direct current of I=10mA, supplied from a series of lead-acid batteries, was used to bias the sensors. The noise was amplified by 40 dB using an HMS Electronics Model 565 low-noise amplifier before being recorded by a HP 35670A spectrum analyzer. The inherent Johnson noise level of the amplifier was 1.24 $nVHz^{-0.5}$. Two overlapping frequency ranges were used during the measurements; 125 mHz to 200 Hz and 8 Hz to 12.8 kHz. The noise measurements set-up is described in detail in reference [30].

Analytical model

It is not obvious how different parameters – length, width, thickness, bias current etc. – influence the sensitivity and detectivity of a PHEB. For example, H_{ex}, H_K, H_d, and $\Delta\rho$ all depend on t_{FM} but in different ways. An analytical model was therefore constructed in order to visualise how the different parameters influenced the performance of the bridge. The validity of the model was verified by comparing the analytical results to experimental data obtained from measurements on the PHEB sensors A1-7 and B1-7.

The dependency of $\Delta\rho$ on t_{FM} was first modelled as in reference [30] by $\Delta\rho$=0.186t_{FM} Ωm. Of the two sets of PHEBs used to verify the model, set B had a slightly lower AMR than predicted by the model and the relation for $\Delta\rho$ was adjusted to $\Delta\rho$=0.151t_{FM} Ωm to account for this discrepancy. The model for $\Delta\rho$ was only valid for relatively small thicknesses, up to around 50 nm [29], since $\Delta\rho$ eventually saturates as t_{FM} increases. However, the maximum thickness of the NiFe layer was limited by the ability of the exchange bias to maintain the single domain configuration and, since this limit

is in the same thickness range, the maximum thickness of this study was set at 50 nm.

The resistivity of the PHEBs was assumed to be equal to the resistivity of the NiFe layer, $\rho_{\text{Ni-Fe}}$=0.183 μΩm, given that $\rho_{\text{Ni-Fe}}<<\rho_{\text{Mn-Ir}}<\rho_{\text{Ta}}$ [35]. Similarly, the charge-carrier density, n_C, of the PHEBs was estimated from the charge-carrier density of $Ni_{80}Fe_{20}$, $n_{\text{Ni-Fe}}$ =17×10^{28} m^{-3} [36], assuming that the main part of the current was conducted through the NiFe layer. The Hooge parameter, γ_H=0.016 was taken from reference [30].

The dependency of H_{ex} and H_K on t_{FM} was modelled as in reference [29] by curve fitting to the reported data. Both fields followed a $(t_{FM})^{-1}$-dependence and the best curve fits were:

$$\begin{aligned}\mu_0 H_{\text{ex}}[\text{T}] &= 9.3\times10^{-11} t_{\text{FM}}^{-1} - 4.3\times10^{-4} \\ \mu_0 H_{\text{K}}[\text{T}] &= 1.7\times10^{-11} t_{\text{FM}}^{-1} - 5.5\times10^{-5}\end{aligned}. \tag{8}$$

The demagnetizing field does not only depend on t_{FM} but also on l and w. For a rectangular prism such as the branches of a PHEB, H_d can be approximated from the equivalent ellipsoid of the prism according to:

$$\mu_0 H_{\text{d}}(l,w,t_{\text{FM}}) = \mu_0 M_{\text{S}}\left(N_{\text{l}}(l,w,t_{\text{FM}}) - N_{\text{w}}(l,w,t_{\text{FM}})\right), \tag{7}$$

where $\mu_0 M_S$=1 T is the saturation magnetization of $Ni_{80}Fe_{20}$, and N_l and N_w are the demagnetization factors along the length and width of the prism, respectively. The demagnetization factors of the PHEBs were calculated as described in reference [37]. The demagnetizing field follows a $t_{FM}w^{-1}$-dependence and is found to be more or less independent of l when $t_{FM}<<w<<l$. It should be noted though that the expression for the sensitivity, equation (4), was derived assuming a cross-shaped sensor design, which when applied to the PHEB sensor design overestimates the significance of the demagnetizing field. This in turn implies that both Σ and D_B will be underestimated.

The overall dependence of D_B on m, n, l, w, and t_{FM} varied depending on if H_{ex} or H_d dominated the magnetization process, if S_T or $S_{1/f}$ dominated the noise spectrum, and if the current or the current density, $J=I(mwt_{FM})^{-1}$, was assumed to be constant. All these dependencies, calculated from curve fitting to the model, are presented in table 2.

Table 2. Dependencies of D_B on the different parameters in the analytical model.

		Low f		High f	
		Constant J	Constant I	Constant J	Constant I
H_{ex} dominates		$(mnl)^{-0.5}$	$(mnl)^{-0.5}$	$(mnl)^{-0.5}$	$m^{0.5}(nl)^{-0.5}$
		$w^{-0.5}$	$w^{-0.5}$	$w^{-0.5}$	$w^{0.5}$
		$t_{FM}^{-2.6}$	$t_{FM}^{-2.6}$	$t_{FM}^{-2.6}$	$t_{FM}^{-1.6}$
H_d dominates		$(mnl)^{-0.5}$	$(mnl)^{-0.5}$	$(mnl)^{-0.5}$	$m^{0.5}(nl)^{-0.5}$
		$w^{-1.4}$	$w^{-1.4}$	$w^{-1.4}$	$w^{-0.4}$
		$t_{FM}^{-0.6}$	$t_{FM}^{-0.6}$	$t_{FM}^{-0.6}$	$t_{FM}^{0.4}$

In table 2, the lower left quadrant includes the largest amount of approximations (H_d, $\Delta\rho$, ρ, n_C, and γ_H) and data from this region should be assumed to be the least reliable. The upper right quadrant, on the other hand, includes the least amount of approximations (H_{ex}, H_K, $\Delta\rho$, and ρ) and data from this region is therefore deemed to be the most reliable. Modelled Σ and D_B of a PHEB with t_{FM} between 20 nm and 50 nm, nl between 100 µm and 265 mm, w=30 µm, m=1, I=10 mA, and f=10 Hz are presented in figure 3.

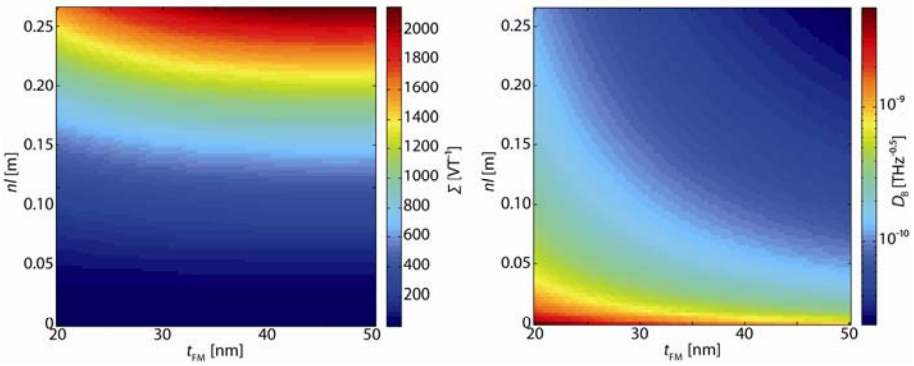

Figure 3. (Colour online) Predicted Σ (left) and D_B at 10 Hz (right) of a PHEB with w=30 µm as a function of nl and t_{FM}.

Verification

The reliability of the analytical model was verified by comparing the modelled data results obtained form actual measurements. The modelled detectivity of the PHEBs A1-A7 agreed well with the measurements (figure 4), although the model slightly underestimated the detectivity at low frequencies. The mean deviation in D_B between the model and the measurements was 2.4% at 10 Hz.

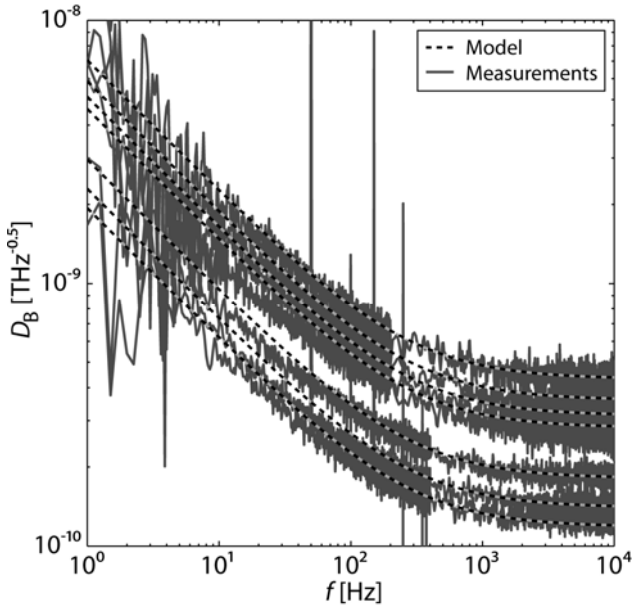

Figure 4. Analytical and measured D_B of PHEBs A1-A7.

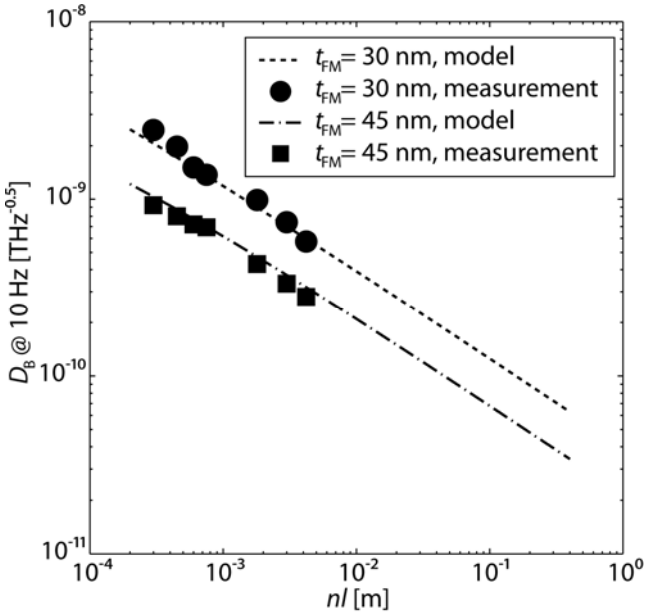

Figure 5. Dependency of D_B at 10 Hz on Nl for PHEBs A10-A140 and B10-B140 as well as corresponding data from the analytical model.

The dependency of the D_B at 10 Hz on Nl for PHEBs A1-A7 and B1-B7 as well as model data for PHEBs with l spanning from 0.1-4 mm and n from 2-100 (m=1), and thicknesses of either t_{FM}=30 nm or t_{FM}=45 nm, are presented in figure 5. The model continued to underestimate D_B as the thickness in-

creased, as expected from the overestimated significance of H_d in the expression for the sensitivity. The mean deviation between the model and the measurements for PHEBs B1-B7 was 9.6%, after the deviation in $\Delta\rho$ had been accounted for.

Hence, the theoretical model should not be expected to deliver exact results for, e.g., D_B, especially at low frequencies and at dimensions where the effect of the demagnetization field on the sensitivity is expected to be large. Nevertheless, the modelled data is in the correct order of magnitude, and the model can therefore be used to estimate the performance of a certain PHEB design, or to guide the optimization of a bridge to meet certain application requirements.

Design

In an application, the PHEBs will be integrated into a system, including supporting structures (e.g. a microfluidic system or a boom for lab-on-a-chip and space applications, respectively) as well as electronics. The latter typically consists of a buffer stage and a preamplifier for isolating the signal, along with an analogue-to-digital converter, and a data acquisition unit.

When designing a PHEB for a particular magnetometer, there are a number of requirements that have to be specified before choosing the geometry of the bridge. In particular, the frequency bandwidth, f_{min}-f_{max}, and the detectivity at f_{min}, $D_{B,min}$, are important. Moreover, the supply voltage, V_S, and the internal noise of the buffer stage and the pre-amplifiers, S_{Amp}, will also affect the design. Here the designs of three magnetometers, labelled MGM1-MGM3, are discussed. The requirement specifications of the magnetometers are presented in table 3.

Table 3. Requirement specifications of MGM1-MGM3.

	f_{min}-f_{max}	$D_{B\,min}$	V_S	S_{Amp}
MGM1	0.1 Hz – 10 kHz	0.1 nTHz-0.5@0.1 Hz	5 V	1 nVHz$^{-0.5}$
MGM2	1 Hz – 10 kHz	0.1 nTHz-0.5@1 Hz	5 V	1 nVHz$^{-0.5}$
MGM3	10 Hz – 10 kHz	0.1 nTHz-0.5@10 Hz	5 V	1 nVHz$^{-0.5}$

The first step of the design process was to define t_{FM} and, since an increase of t_{FM} is the most effective measure to suppress both $S_{1/f}$ and S_T, it should be made as large as possible. The maximum thickness was, as already mentioned, around 50 nm.

Due to different dependencies of the detectivity on size (table 2) and bias current in the high and low frequency regions, there are two ways to approach the remaining part of the bridge design, depending on if the bridge is to be, either as small, or as power efficient as possible.

The low frequency detectivity is independent of I and can only be improved by increasing the dimensions of the bridge. Hence, the smallest

bridge possible fulfilling the requirement set by $D_{B\,min}$ can be found by making the 1/*f*-region of D_B dominant at f_{min}. In reality this means that the frequency independent part of the detectivity (the high frequency region) should be suppressed by increasing *I*, resulting in high power consumption.

If, instead, low power consumption is required, the bias current should be kept small. The minimum current fulfilling the requirement set by $D_{B\,min}$ can in this case be found by making the frequency independent part of D_B dominant at f_{min}. Contrary to the previous case of minimum size, this requires that the significance of the low frequency 1/*f* region of the detectivity is suppressed by increasing the size of the bridge.

Depending on the design, the current density *J* can be calculated at f_{min}, assuming either $S_{1/f}\,\Sigma^{-1} \geq 10\,S_T\,\Sigma^{-1}$ in the minimum size case or $S_T\,\Sigma^{-1} \geq 10\,S_{1/f}\,\Sigma^{-1}$ in the minimum power case, yielding:

$$J_{size} = \sqrt{40 k_B T n_c f_{min} (\rho \gamma_H)^{-1}}\,, \tag{8}$$

$$J_{power} = \sqrt{4 k_B T n_c f_{min} (10 \rho \gamma_H)^{-1}}\,, \tag{9}$$

where J_{size} and J_{power} are the current densities in the minimum size and minimum power cases, respectively.

With *J* defined as either J_{size} or J_{power}, *l*, *w*, and *N* can be calculated from the theoretical model. The relationship between these three parameters differs somewhat depending on which design was chosen for the bridge (figure 2). For the denser design (figure 2 (b)), *N* is the largest integer fulfilling

$N < l(w+p)^{-1}$, if the footprint of each branch is to be quadratic. According to the requirements, D_B should be less than $D_{B,min}$ at f_{min}. Another requirement is that S_{Amp} should be smaller than S_V so that the bridge signal is not hidden by amplifier noise. A reasonable requirement is that $S_V \geq 10\,S_{Amp}$. Many sets of (*l*,*w*, *N*) fulfil these two requirements but it was convenient to choose the set with the smallest *l* (figure 6).

With *N* defined, *n* could be determined from the supply voltage V_S, by using $V_S > IR = J\rho nl$ and

$$n < V_S (Jl\rho)^{-1}, \tag{10}$$

where, *n* is the largest integer fulfilling the condition. Finally, *m* was defined so that $m \geq Nn^{-1}$. Now, the power consumption, $P = I^2R = J^2\rho nlmwt_{FM}$, and the area of the whole PHEB could be calculated. The total area was approximately $l(l+4N(w+p))$ for design (a), and $4l^2$ for design (b) in figure 2, respectively.

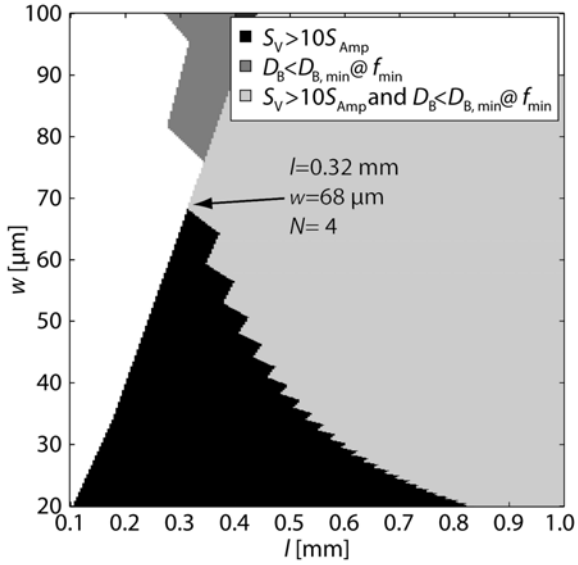

Figure 6. Sets of l, w, and N that fulfil the requirements of MGM3 in the minimum size design.

By applying this design process to the requirements of MGM1-MGM3 (table 3), the magnetometers size, sensitivity, resistance, bias current and power consumption could be calculated, table 4. The resulting D_B spectrum of the magnetometers are presented in figure 7. For comparison to figure 1, D_B at 1 Hz was 43 pTHz$^{-0.5}$, 100 pTHz$^{-0.5}$ and 300 pTHz$^{-0.5}$ for MGM1-MGM3, respectively.

Of the three magnetometers, MGM3 was the most influenced by demagnetizing effects, the ratio between the anisotropy fields being $H_d(H_{ex}+H_k)^{-1}$=2.0. For MGM1 and MGM2 this ratio was 0.50 and 1.0, respectively. Hence, the expression used for the sensitivity, equation (4), overestimating the significance of H_d in case of PHEB sensors should not have too much negative impact on the calculated data and the theoretical model can therefore be used as a reliable design tool.

Table 4. Properties of MGM1-MGM3 aiming at minimum size (top) and minimum power (bottom).

Minimum size	J_{size} [Am^{-2}]	l [mm]	w [µm]	n	m	Σ [V/T]	R [Ω]	I [mA]	P [mW]	A [mm^2]
MGM1	$9.6\cdot10^8$	1.8	440	4	1	33	60	21	27	13
MGM2	$3.1\cdot10^9$	0.71	165	4	1	33	60	25	40	2.0
MGM3	$9.6\cdot10^9$	0.32	68	4	1	35	68	33	74	0.41
Minimum power	J_{power} [Am^{-2}]	l [mm]	w [µm]	n	m	Σ [V/T]	R [Ω]	I [mA]	P [mW]	A [mm^2]
MGM1	$9.6\cdot10^7$	6.0	460	12	1	32	570	2.2	2.8	144
MGM2	$3.1\cdot10^8$	2.3	180	12	1	32	570	2.7	4.3	21
MGM3	$9.6\cdot10^8$	1.0	76	12	1	32	600	3.7	8.0	4.0

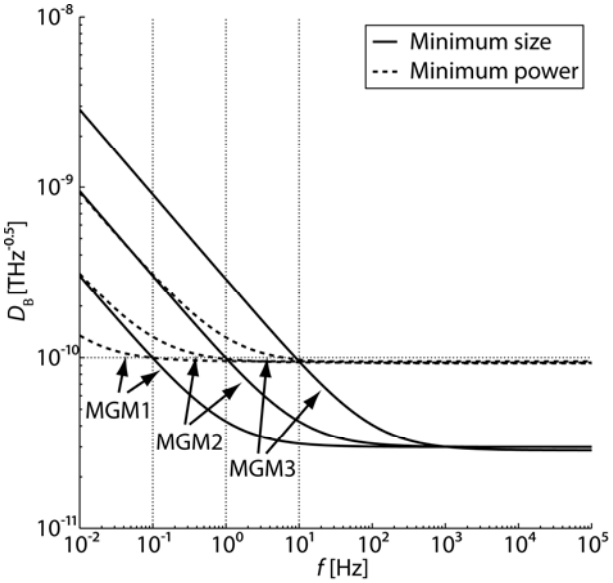

Figure 7. D_B of MGM1-MGM3 with requirements from table 3 and parameters from table 4.

Conclusion

Summarizing, a theoretical model to estimate the detectivity of an arbitrary PHEB was evaluated, and a design process to optimize the dimensions of such a bridge, given certain sensor requirement, was developed. The model employed a number of approximations, such as the expression used to calculate the sensitivity which overestimates the significance of the demagnetization field, but still proved to generate reasonably accurate data. However, the model is sensitive to fabrication process induced variations of the material properties of the thin films, e.g. in the anisotropic magnetoresistance. Nevertheless, by improved control of the fabrication process and by employing, e.g., post-annealing of the samples [38, 39], the variations of these properties can be expected to diminish, making the model even more useful as a design tool for PHEB magnetometers.

Even though the model did not produce exact data for, e.g., the detectivity, the results are still in the correct order of magnitude, and the approximations were assumed to underestimate the performance of the sensors. Hence, the model can be used to guide the design of a PHEB and to optimize given certain sensor requirements. Optimization in terms of length, width, thickness, etc. can follow two paths aiming for the bridge being either as small or as power efficient as possible. This design process can be a useful tool for investigating the applicability of PHEBs in different science areas where there is a need for magnetic field measurements.

The modelled performances of MGM1-MGM3 show that PHEBs are potentially applicable to a large number of science areas. Comparing with figure 1, they are already applicable to e.g. magnetic bio detection and satellite attitude determination but, MGM1 also has potential for archaeological surveying and for scientific space missions studying, e.g., the magnetosphere.

References

[1] Zhongguo ke xue ji shu bo wu g 1983 China, 7000 years of discovery: China's ancient technology China reconstructs magazine

[2] Racz R, C Schott and S Huber 2004 Electronic compass sensor 1446-9 vol.3

[3] Schott C, R Racz, A Manco and N Simonne 2007 CMOS Single-Chip Electronic Compass With Microcontroller *Solid-State Circuits, IEEE Journal of* **42** 2923-33

[4] Gaffney C 2008 Detecting Trends in the Prediction of the Buried Past: A Review of Geophysical Techniques in Archaeology *Archaeometry* **50** 313-36

[5] Rogers M B, K Faehndrich, B Roth and G Shear 2010 Cesium magnetometer surveys at a Pithouse Site near Silver City, New Mexico *Journal of Archaeological Science* **37** 1102-9

[6] Acuna M H 2002 Space-based magnetometers *Review of Scientific Instruments* **73** 3717-36

[7] Auster H, K Glassmeier, W Magnes, O Aydogar, W Baumjohann, D Constantinescu, D Fischer, K Fornacon, E Georgescu, P Harvey, O Hillenmaier, R Kroth, M Ludlam, Y Narita, R Nakamura, K Okrafka, F Plaschke, I Richter, H Schwarzl, B Stoll, A Valavanoglou and M Wiedemann 2008 The THEMIS Fluxgate Magnetometer *Space Science Reviews* **141** 235-64

[8] O' Brien H, P Brown, T Beek, C Carr, E Cupido and T Oddy 2007 A radiation tolerant digital fluxgate magnetometer *Measurement Science and Technology* **18** 3645

[9] Haun J B, T-J Yoon, H Lee and R Weissleder 2010 Magnetic nanoparticle biosensors *Wiley Interdisciplinary Reviews: Nanomedicine and Nanobiotechnology* **2** 291-304

[10] Llandro J, J Palfreyman, A Ionescu and C Barnes 2010 Magnetic biosensor technologies for medical applications: a review *Medical and Biological Engineering and Computing* **48** 977-98

[11] Forslund A, S Belyayev, N Ivchenko, G Olsson, T Edberg and A Marusenkov 2008 Miniaturized digital fluxgate magnetometer for small spacecraft applications *Measurement Science & Technology* **19** 015202-1

[12] Griffith W C, R Jimenez-Martinez, V Shah, S Knappe and J Kitching 2009 Miniature atomic magnetometer integrated with flux concentrators *Applied Physics Letters* **94** 023502 (3 pp.)

[13] Freitas P P, R Ferreira, S Cardoso and F Cardoso 2007 Magnetoresistive sensors *Journal of Physics: Condensed Matter* **19** 21 pp.

[14] Michelena M D, I Arruego, J M Oter and H Guerrero 2010 COTS-Based Wireless Magnetic Sensor for Small Satellites *IEEE Transactions on Aerospace and Electronic Systems* **46** 542-57

[15] Michelena M D, W Oelschlagel, I Arruego, R P del Real, J A D Mateos and J M Merayo 2008 Magnetic giant magnetoresistance commercial off the shelf for space applications *Journal of Applied Physics* **103** 07-912

[16]Persson A, G Thornell and H Nguyen 2011 Radiation tolerance of a spin-dependent tunnelling magnetometer for space applications *Measurement Science and Technology* **22** 045204
[17]Díaz-Michelena M 2009 Small Magnetic Sensors for Space Applications *Sensors* **9** 2271-88
[18]Hass K J, G W Donohoe, Y K Hong and B C Choi 2006 Magnetic Flip Flops for Space Applications *Magnetics, IEEE Transactions on* **42** 2751-3
[19]Sundkvist D, V Krasnoselskikh, P K Shukla, A Vaivads, M Andre, S Buchert and H Reme 2005 In situ multi-satellite detection of coherent vortices as a manifestation of Alfvenic turbulence *Nature* **436** 825-8
[20]Endimiani A, K M Hujer, A M Hujer, S Kurz, M R Jacobs, D S Perlin and R A Bonomo 2011 Are We Ready for Novel Detection Methods to Treat Respiratory Pathogens in Hospital-Acquired Pneumonia? *Clinical Infectious Diseases* **52** S373-S83
[21]Teles F R R and L P Fonseca 2008 Trends in DNA biosensors *Talanta* **77** 606-23
[22]Dave S R and X Gao 2009 Monodisperse magnetic nanoparticles for biodetection, imaging, and drug delivery: a versatile and evolving technology *Wiley Interdisciplinary Reviews: Nanomedicine and Nanobiotechnology* **1** 583-609
[23]Göransson J, T Zardán Gómez De La Torre, M Strömberg, C Russell, P Svedlindh, M Strømme and M Nilsson 2010 Sensitive Detection of Bacterial DNA by Magnetic Nanoparticles *Analytical Chemistry* **82** 9138-40
[24]Strömberg M, J Göransson, K Gunnarsson, M Nilsson, P Svedlindh and M Strømme 2008 Sensitive Molecular Diagnostics Using Volume-Amplified Magnetic Nanobeads *Nano Letters* **8** 816-21
[25]Dalslet B T, C D Damsgaard, M Donolato, M Stromme, M Stromberg, P Svedlindh and M F Hansen 2011 Bead magnetorelaxometry with an on-chip magnetoresistive sensor *Lab on a Chip* **11** 296-302
[26]Osterberg F W, B T Dalslet, D Snakenborg, C Johansson and M F Hansen 2010 Chip-Based Measurements of Brownian Relaxation of Magnetic Beads Using a Planar Hall Effect Magnetic Field Sensor *AIP Conference Proceedings* **1311** 176-83
[27]McGuire T and R Potter 1975 Anisotropic magnetoresistance in ferromagnetic 3d alloys *Magnetics, IEEE Transactions on* **11** 1018-38
[28]Schuhl A, F N Van Dau and J R Childress 1995 Low-field magnetic sensors based on the planar Hall effect *Applied Physics Letters* **66** 2751-3
[29]Damsgaard C D, S C Freitas, P P Freitas and M F Hansen 2008 Exchange-biased planar Hall effect sensor optimized for biosensor applications *Journal of Applied Physics* **103** 07-302
[30]Persson A, R Bejhed, H Nguyen, K Gunnarsson, B T Dalslet, F W Østerberg and M F Hansen 2011 Low-frequency noise in planar Hall effect bridge sensors *Sensors and Actuators A* **submitted**
[31]Henriksen A D, B T Dalslet, D H Skieller, K H Lee, F Okkels and M F Hansen 2010 Planar Hall effect bridge magnetic field sensors *Applied Physics Letters* **97** 013507 (3 pp.)
[32]Donolato M, B T Dalslet, C D Damsgaard, K Gunnarsson, C S Jacobsen, P Svedlindh and M F Hansen 2011 Size-dependent effects in exchange-biased planar Hall effect sensor crosses *Journal of Applied Physics* **109** 064511-9
[33]Johnson J B 1928 Thermal Agitation of Electricity in Conductors *Physical Review* **32** 97
[34]Hooge F N 1976 1/f noise **83B+C** 14-23

[35]Gehanno V, P P Freitas, A Veloso, J Ferrira, B Almeida, J B Soasa, A Kling, J C Soares and M F da Silva 1999 Ion beam deposition of Mn-Ir spin valves *IEEE Transactions on Magnetics* **35** 4361-7
[36]Briaire J, L K J Vandamme and M A M Gijs 1997 Resistance and 1/f noise dependence on magnetic field in single Ni80Fe20 layers and Ni80Fe20/Cu multilayers 587-90
[37]Beleggia M and et al. 2006 The equivalent ellipsoid of a magnetized body *Journal of Physics D: Applied Physics* **39** 891
[38]Anderson G W, Y Huai and M Pakala 2000 Spin-valve thermal stability: The effect of different antiferromagnets *Journal of Applied Physics* **87** 5726-8
[39]Sun J J, K Shimazawa, N Kasahara, K Sato, S Saruki, T Kagami, O Redon, S Araki, H Morita and M Matsuzaki 2000 Low resistance and high thermal stability of spin-dependent tunnel junctions with synthetic antiferromagnetic CoFe/Ru/CoFe pinned layers *Applied Physics Letters* **76** 2424-6